

# Time-Asymmetric Protocol Optimization for Efficient Free Energy Estimation

Adrienne Zhong\* and Benjamin Kuznets-Speck\*

Department of Physics, University of California, Berkeley, CA, 94720, USA and  
Biophysics Graduate Group, University of California, Berkeley, CA, 94720, USA

Michael R. DeWeese

Department of Physics, University of California, Berkeley, CA, 94720 and  
Redwood Center For Theoretical Neuroscience and Helen Wills Neuroscience Institute,  
University of California, Berkeley, Berkeley, CA, 94720

(Dated: November 27, 2023)

The free-energy difference  $\Delta F$  between two high-dimensional systems is notoriously difficult to compute, but very important for many applications, such as drug discovery [1]. We demonstrate that the microscopic fluctuation theorem for an unconventional definition of work introduced by Vaikuntanathan and Jarzynski (2008) connects path ensembles that are driven by protocols unequal under time-reversal, allowing us to use a low-variance Bennett acceptance ratio  $\Delta F$  estimator on bi-directional measurements from time-asymmetric processes. It has been shown before that counterdiabatic protocols give zero-variance work measurements for this definition. Motivated by this, we propose an on-the-fly adaptive importance sampling policy optimization algorithm that iteratively improves the efficiency of the time-asymmetric protocols. This algorithm requires minimal computational overhead, and uses all the samples collected in previous iterations to (1) update the protocol, and (2) provide a  $\Delta F$  estimate. We test our algorithm on three models of varying complexity, finding that with just  $10^3$  bi-directional work samples our algorithm yields  $\Delta F$  estimates that are  $\sim 10^2 - 10^4$  times lower in mean squared error than the linear interpolation protocol with which it was initialized.

Free energy differences  $\Delta F = F_B - F_A$  between pairs of potential energy functions  $U_A(\mathbf{x})$  and  $U_B(\mathbf{x})$  are sought after by physicists, chemists, and pharmaceutical scientists alike [1–6]. Here,  $\mathbf{x} \in \mathbb{R}^d$  is the configuration space coordinate, and the free energy for each potential is defined as  $F_{A,B} = -\beta^{-1} \ln \int e^{-\beta U_{A,B}(\mathbf{x}')} d\mathbf{x}'$ , where  $\beta = (k_B T)^{-1}$  is inverse temperature. For high dimensional systems,  $\Delta F$  can only be calculated numerically through sampling methods, which can be computationally costly and slow to converge [4]. Here we develop an adaptive method to learn efficient finite-time protocols that approximate a counterdiabatic force that estimates  $\Delta F$  with zero variance.

One class of estimators takes work measurements as input from protocols  $U(\mathbf{x}, t)$  that “switch”  $U(\mathbf{x}, 0) = U_A(\mathbf{x}) \rightarrow U(\mathbf{x}, t_f) = U_B(\mathbf{x})$  in finite time  $t_f$ . Because the work, traditionally defined for each trajectory  $\mathbf{x}(t)|_{t \in [0, t_f]}$  as

$$W_{\text{trad}}[\mathbf{x}(t)] = \int_0^{t_f} \frac{\partial U}{\partial t}(\mathbf{x}(t), t) dt \quad (1)$$

satisfies the Jarzynski equality

$$\langle e^{-\beta W} \rangle = e^{-\beta \Delta F}, \quad (2)$$

the Jarzynski estimator  $\widehat{\Delta F}_{\text{Jar}} = -\beta^{-1} \ln (n_s^{-1} \sum_{i=1}^{n_s} e^{-\beta W_{\text{trad}}^i})$  may be applied to work measurements  $\{W_{\text{trad}}^i, |i = 1, \dots, n_s\}$ . Unfortunately

this estimator can be slow to converge, because the average is often dominated by rare events.

Estimators that use bi-directional work measurements (i.e., those that also consider  $U_B \rightarrow U_A$  switching processes) generally have lower variance than uni-directional work estimators [7]. In particular, Shirts et al. in [8] showed that if forward  $\{W_F^i | i = 1, \dots, n_s\}$  and reverse work measurements  $\{W_R^i | i = 1, \dots, n_s\}$ , assumed here to be equal in number for simplicity, are collected from forward and reverse protocols satisfying Crooks Fluctuation Theorem

$$P_F(+W) = P_R(-W) e^{\beta(W - \Delta F)}, \quad (3)$$

then the Bennett acceptance ratio estimator  $\widehat{\Delta F}_{\text{BAR}}$  [9], defined implicitly as the  $\Delta F$  satisfying

$$\sum_{i=1}^{n_s} \frac{1}{1 + e^{-\beta(W_F^i - \Delta F)}} - \sum_{j=1}^{n_s} \frac{1}{1 + e^{-\beta(W_R^j + \Delta F)}} = 0, \quad (4)$$

is the lowest-variance asymptotically-unbiased estimator. Bi-directional measurements of  $W_{\text{trad}}$  for a pair of time-reversal-symmetric forward and reverse protocols satisfy Eq. (3) [10, 11], but measurements can also be collected from *mixtures* of different measurement-protocol pairs

$$P_F(\cdot) = \sum_i \alpha_i P_F^i(\cdot) \quad \text{and} \quad P_R(\cdot) = \sum_i \alpha_i P_R^i(\cdot) \quad (5)$$

with  $\sum_i \alpha_i = 1$ , as long as each  $(P_F^i, P_R^i)$  pair satisfies Eq. (3).

In this Letter, we consider the non-standard definition of work introduced in [12], for which there exists finite-time counterdiabatic driving protocols that give zero-variance work measurements. We explicitly show that

\* [adrizhong@berkeley.edu](mailto:adrizhong@berkeley.edu), [biophysben@gmail.com](mailto:biophysben@gmail.com).  
These authors contributed equally.

it satisfies the fluctuation theorem Eq. (3) for measurements that are produced from forward and reverse protocols that are *unequal* under time-reversal. We propose an algorithm that iteratively improves time-asymmetric protocols from bi-directional measurements collected across all iterations. Finally, for three examples of increasing complexity, we demonstrate that  $10^3$  bi-directional measurements made under our protocol optimization algorithm give  $\Delta F$  estimates that are a factor of  $\sim 10^2 - 10^4$  lower in mean squared error than  $10^3$  bi-directional measurements made with the naive linear interpolation protocol with which it was initialized.

*Time-asymmetric work.*—For our setting we consider a time-varying potential energy  $U_0(\mathbf{x}, t)$  for  $t \in [0, t_f]$ , that begins at  $U_0(\mathbf{x}, 0) = U_A(\mathbf{x})$  and ends at  $U_0(\mathbf{x}, t_f) = U_B(\mathbf{x})$ . To this we add an additional potential  $U_1(\mathbf{x}, t)$  that satisfies  $U_1(\mathbf{x}, 0) = U_1(\mathbf{x}, t_f) = 0$ . In the over-damped limit,  $\mathbf{x}(t)$  evolves under the Langevin equation

$$\dot{\mathbf{x}} = -\nabla(U_0 + U_1) + \sqrt{2\beta^{-1}} \boldsymbol{\eta}(t) \quad \text{with} \quad \mathbf{x}(0) \sim \rho_A(\cdot). \quad (6)$$

Here,  $\rho_A(\mathbf{x}) = e^{-\beta[U_A(\mathbf{x}) - F_A]}$  is the equilibrium distribution for  $U_A(\mathbf{x})$ , and  $\boldsymbol{\eta}(t)$  is an instantiation of standard  $d$ -dimensional Gaussian white noise specified by  $\langle \eta_i(t) \rangle = 0$  and  $\langle \eta_i(t) \eta_j(t') \rangle = \delta_{ij} \delta(t - t')$  [13].

In [12] the authors introduced the non-conventional work definition, which in our setting is

$$W[\mathbf{x}(t)] = \int_0^{t_f} \frac{\partial U_0}{\partial t} - \nabla U_0 \cdot \nabla U_1 + \beta^{-1} \nabla^2 U_1 dt \quad (7)$$

( $\nabla^2$  is the scalar Laplace operator), and demonstrated that, remarkably,  $W[\mathbf{x}(t)] = \Delta F$  for *every* trajectory  $\mathbf{x}(t)$ , if  $U_1(\mathbf{x}, t)$  gives the counterdiabatic force for  $U_0(\mathbf{x}, t)$ , meaning

$$\frac{\partial \rho_0}{\partial t} = \nabla \cdot (\rho_0 \nabla U_1) \quad \text{for} \quad \rho_0(\mathbf{x}, t) := e^{-\beta[U_0(\mathbf{x}, t) - F_0(t)]}. \quad (8)$$

Here  $\rho_0(\mathbf{x}, t)$  is the instantaneous equilibrium distribution corresponding to  $U_0(\mathbf{x}, t)$ , with time-dependent free energy  $F_0(t) = -\beta^{-1} \ln \int e^{-\beta U_0(\mathbf{x}', t)} d\mathbf{x}'$  satisfying  $F_0(0) = F_A$  and  $F_0(t_f) = F_B$  [14–16]. Under these conditions, the time-dependent probability distribution for Eq. (6) is always in instantaneous equilibrium with  $U_0(\mathbf{x}, t)$ .

Indeed, expanding Eq. (8) yields

$$\frac{\partial U_0}{\partial t} - \nabla U_0 \cdot \nabla U_1 + \beta^{-1} \nabla^2 U_1 = \frac{dF_0}{dt}, \quad (9)$$

which, when plugged into Eq. (7), shows that the time-asymmetric work  $W[\mathbf{x}(t)] = \int_0^{t_f} \dot{F}_0(t) dt = F_0(t_f) - F_0(0) = \Delta F$  for *every* trajectory  $\mathbf{x}(t)$ . With optimally chosen  $U_0(\mathbf{x}, t)$  and  $U_1(\mathbf{x}, t)$ , the free energy difference may be obtained from simulating a single finite-time trajectory. Unfortunately, Eq. (9) is typically infeasible to solve for multidimensional systems, and to formulate the PDE,  $\dot{F}_0(t)$ , and therefore  $\Delta F$ , must already be known.

*Microscopic fluctuation theorem*—In the late 1990s, Crooks [10, 11] discovered that the microscopic fluctuation theorem

$$W[\mathbf{x}(t)] = \Delta F + \beta^{-1} \ln \frac{P[\mathbf{x}(t)]}{\tilde{P}[\tilde{\mathbf{x}}(t)]} \quad (10)$$

is satisfied by the traditional work  $W = W_{\text{trad}}$ . Here  $P[\mathbf{x}(t)]$  is the probability of observing a trajectory  $\mathbf{x}(t)$ , and  $\tilde{P}[\tilde{\mathbf{x}}(t)]$  is the probability of observing its time-reversed trajectory  $\tilde{\mathbf{x}}(t) = \mathbf{x}(t_f - t)$  in a “reverse” path ensemble driven by the protocol  $\tilde{U}(\mathbf{x}, t) = U(\mathbf{x}, t_f - t)$ . In order to gain insight into the non-conventional work definition Eq. (7), we examine its associated microscopic fluctuation theorem.

In our overdamped setting, the probability of realizing a trajectory  $\mathbf{x}(t)$  from the dynamics Eq. (6) may be formally expressed, up to a normalization factor, as

$$P[\mathbf{x}(t)] = \rho_A(\mathbf{x}(0)) e^{-\beta S[\mathbf{x}(t)]}, \quad (11)$$

where

$$S[\mathbf{x}(t)] = (\text{I}) \int_0^{t_f} \frac{|\dot{\mathbf{x}} + \nabla(U_0 + U_1)|^2}{4} dt, \quad (12)$$

is the Onsager-Machlup action functional (which we derive in Appendix Sec. A 1, also see [17]). We use (I) to indicate that the integral is taken in an Itô sense (reviewed in Appendix Sec. A 2). After Eqs. (7) and (11) are plugged into Eq. (10), straightforward manipulations under the rules of stochastic calculus (see Appendix Sec. A 3) yield

$$\begin{aligned} \tilde{P}[\tilde{\mathbf{x}}(t)] &= e^{-\beta\{U_A(\mathbf{x}(0)) - F_A + S[\mathbf{x}(t)] + W[\mathbf{x}(t)] - \Delta F\}} \\ &= \rho_B(\tilde{\mathbf{x}}(0)) e^{-\beta \tilde{S}[\tilde{\mathbf{x}}(t)]}, \end{aligned} \quad (13)$$

where  $\rho_B(\mathbf{x}) = e^{-\beta[U_B(\mathbf{x}) - F_B]}$  is the equilibrium distribution for  $U_B(\mathbf{x})$ , and

$$\tilde{S}[\tilde{\mathbf{x}}(t)] = (\text{I}) \int_0^{t_f} \frac{|\dot{\tilde{\mathbf{x}}} + \nabla(\tilde{U}_0 - \tilde{U}_1)|^2}{4} dt \quad (14)$$

has the form of a path action, with  $\tilde{U}_{0,1}(\mathbf{x}, t) = U_{0,1}(\mathbf{x}, t_f - t)$  denoting the time-reversed potential energies. Eq. (13) gives the probability of observing the path  $\tilde{\mathbf{x}}(t)$  under the Langevin equation

$$\dot{\tilde{\mathbf{x}}} = -\nabla(\tilde{U}_0 - \tilde{U}_1) + \sqrt{2\beta^{-1}} \boldsymbol{\eta}(t) \quad \text{with} \quad \tilde{\mathbf{x}}(0) \sim \rho_B(\cdot), \quad (15)$$

differing from Eq. (6) by a minus sign on the  $U_1$  term. In other words, the reverse path ensemble that satisfies Eq. (13) for the time-asymmetric work Eq. (7) is one that is driven by a protocol  $\tilde{U}_0 - \tilde{U}_1$  that is *different* from the time-reversal of the forward protocol  $U_0 + U_1$ . One can also verify that its associated definition of work

$$\tilde{W}[\tilde{\mathbf{x}}(t)] = \int_0^{t_f} \frac{\partial \tilde{U}_0}{\partial t} - \nabla \tilde{U}_0 \cdot \nabla(-\tilde{U}_1) + \beta^{-1} \nabla^2(-\tilde{U}_1) dt, \quad (16)$$

satisfies  $\tilde{W}[\tilde{\mathbf{x}}(t)] = -W[\mathbf{x}(t)]$ , so the same optimal  $U_0(\mathbf{x}, t)$  and  $U_1(\mathbf{x}, t)$  satisfying Eq. (8) also give  $\tilde{W}[\tilde{\mathbf{x}}(t)] = -\Delta F$  for every trajectory.

Through standard methods (see Appendix Sec. B), the fluctuation theorem Eq. (3) follows directly from the microscopic fluctuation theorem Eq. (13). Thus, the time-asymmetric work (Eq. (7)) holds a deeper significance than how it may first appear – it relates the forward and reverse path ensembles given by Eqs. (6) and (15) that are driven by time-asymmetric protocols. We now exploit this to efficiently calculate free energy differences.

*Algorithm.*—In this section we present an on-the-fly adaptive importance-sampling protocol optimization algorithm, inspired by [18], that uses the previously collected bi-directional samples to iteratively discover lower-variance time-asymmetric protocols. Exploiting the mathematical structure of the Onsager-Machlup action, our algorithm requires minimal computational overhead, solely the inclusion of easily-computable auxiliary variables in each trajectory’s time-evolution.

Concretely, we consider the objective function

$$J = J_F + J_R = \langle W \rangle_F + \langle \tilde{W} \rangle_R. \quad (17)$$

Jensen’s inequality applied to Eq. (2) implies  $\langle W \rangle_F \geq \Delta F$  and  $\langle \tilde{W} \rangle_R \geq -\Delta F$ , with equality only for zero-variance optimal protocols.

Our simulations are performed using the Euler-Mayurama method to discretize Eqs. (6) and (15). Instead of directly discretizing Eq. (7), we measure for every trajectory the expression derived from Eq. (13)

$$W[\mathbf{x}(t)] = U_B(\mathbf{x}(t_f)) - U_A(\mathbf{x}(0)) + \beta^{-1} \ln \frac{P[\mathbf{x}(t)|\mathbf{x}(0)]}{\tilde{P}[\tilde{\mathbf{x}}(t)|\tilde{\mathbf{x}}(0)]} \quad (18)$$

with the correct discrete-path probabilities, so as to preserve the fluctuation theorem (10). In our setting this may be written as

$$W[\mathbf{x}(t)] = \{U_B(\mathbf{x}(t_f)) + \tilde{S}[\tilde{\mathbf{x}}(t)]\} - \{U_A(\mathbf{x}(0)) + S[\mathbf{x}(t)]\}. \quad (19)$$

From now on we will use Einstein notation, where repeated upper and lower Greek indices signify summation. Let  $\{U_\mu(\mathbf{x}, t) | \mu = 1, \dots, M\}$  denote a set of time-dependent basis functions. Given the linear parameterization of the forward and reverse protocols  $U_F = U_0 + U_1$  and  $U_R = U_0 - U_1$

$$U_{F,R}(\mathbf{x}, t) = \begin{cases} U_A(\mathbf{x}) & \text{for } t = 0 \\ \theta_{F,R}^\mu U_\mu(\mathbf{x}, t) & \text{for } t \in (0, t_f) \\ U_B(\mathbf{x}) & \text{for } t = t_f \end{cases} \quad (20)$$

with parameters  $\theta = (\theta_F, \theta_R) \in \mathbb{R}^{2M}$ , the Onsager-Machlup path action Eq. (12) and the time-asymmetric work Eq. (19) become quadratic in  $\theta$

$$S[\mathbf{x}(t); \theta] = \theta_F^\mu \theta_F^\nu \mathbf{a}_{\mu\nu} + \theta_F^\mu \mathbf{b}_\mu + \theta\text{-ind. terms} \quad (21)$$

$$W[\mathbf{x}(t); \theta] = -(\theta_F^\mu \theta_F^\nu \mathbf{a}_{\mu\nu} + \theta_F^\mu \mathbf{b}_\mu + \mathbf{c}) + (\theta_R^\mu \theta_R^\nu \tilde{\mathbf{a}}_{\mu\nu} + \theta_R^\mu \tilde{\mathbf{b}}_\mu + \tilde{\mathbf{c}}), \quad (22)$$

where

$$\begin{aligned} \mathbf{a}_{\mu\nu}[\mathbf{x}(t)] &= (\text{I}) \int_0^{t_f} \frac{\nabla U_\mu \cdot \nabla U_\nu}{4} dt, & \mathbf{b}_\mu[\mathbf{x}(t)] &= (\text{I}) \int_0^{t_f} \frac{\dot{\mathbf{x}} \cdot \nabla U_\mu}{2} dt, & \mathbf{c}[\mathbf{x}(t)] &= U_A(\mathbf{x}(0)), \\ \tilde{\mathbf{a}}_{\mu\nu}[\mathbf{x}(t)] &= (\text{BI}) \int_0^{t_f} \frac{\nabla U_\mu \cdot \nabla U_\nu}{4} dt, & \tilde{\mathbf{b}}_\mu[\mathbf{x}(t)] &= -(\text{BI}) \int_0^{t_f} \frac{\dot{\mathbf{x}} \cdot \nabla U_\mu}{2} dt, & \text{and } \tilde{\mathbf{c}}[\mathbf{x}(t)] &= U_B(\mathbf{x}(t_f)) \end{aligned} \quad (23)$$

are  $\theta$ -independent functionals of the time-discretized trajectory  $\mathbf{x}(t)$  [19]. Here, (BI) refers to a Backwards Itô integral, needed to write terms of the reverse ensemble  $\tilde{S}[\tilde{\mathbf{x}}(t)]$  as a functional of  $\mathbf{x}(t)$ . (Eqs. (21)–(23) apply for the reverse path ensemble  $\tilde{S}[\tilde{\mathbf{x}}(t)]$ ,  $\tilde{W}[\tilde{\mathbf{x}}(t)]$ , through the transformation  $t \rightarrow t_f - t$ ,  $\{F, R\} \rightarrow \{R, F\}$ .) These variables  $\mathbf{a}, \tilde{\mathbf{a}} \in \mathbb{R}^{M \times M}$ ,  $\mathbf{b}, \tilde{\mathbf{b}} \in \mathbb{R}^M$ , and  $\mathbf{c}, \tilde{\mathbf{c}} \in \mathbb{R}$  are akin to the eligibility trace variables (sometimes called “Malliavin weights”) used in reinforcement learning policy-gradient algorithms [20–24], which are dynamically evolved with each trajectory  $\mathbf{x}(t)$ .

In the following two paragraphs we consider only the

forward ensemble for simplicity. If for every trajectory  $\mathbf{x}^i(t)$ , as well as the work  $W^i$  we calculate its functional values  $(\mathbf{a}^i, \mathbf{b}^i, \mathbf{c}^i, \tilde{\mathbf{a}}^i, \tilde{\mathbf{b}}^i, \tilde{\mathbf{c}}^i)$  and keep track of the  $\theta^i = (\theta_F^i, \theta_R^i)$  under which it was produced, then the  $\theta$ -dependent importance-sampling estimator may be constructed

$$\hat{J}_F(\theta) = \frac{\sum_{i=1}^{n_s} \mathbf{r}_F^i(\theta) \mathbf{w}_F^i(\theta)}{\sum_{i=1}^{n_s} \mathbf{r}_F^i(\theta)}, \quad (24)$$

where the sum is over collected forward samples  $i$ ,  $\mathbf{r}_F^i(\theta)$  is

the likelihood ratio (i.e., the Radon–Nikodym derivative)

$$r_F^i(\theta) = \frac{P[\mathbf{x}^i(t) \text{ from } \theta]}{P[\mathbf{x}^i(t) \text{ from } \theta^i]} = e^{-\beta(S[\mathbf{x}^i(t); \theta] - S[\mathbf{x}^i(t); \theta^i])}, \quad (25)$$

and  $w^i(\theta) = W[\mathbf{x}^i(t); \theta]$  is the time-asymmetric work for the trajectory  $\mathbf{x}^i(t)$  as if it were sampled under  $\theta$  instead of  $\theta^i$ . *The protocol may be optimized by minimizing Eq. (24).*

Of course, the quality of the importance-sampling estimate Eq. (24) degrades the further away the input  $\theta$  is from the set of  $\theta^i$  under which samples were collected. One common heuristic of this degradation is the effective sample size [25]

$$n_F^{\text{eff}}(\theta) = \frac{(\sum_{i=1}^{n_s} r_F^i(\theta))^2}{\sum_{i=1}^{n_s} r_F^i(\theta)^2}, \quad (26)$$

ranging from 1 (uneven  $r_F^i$  values, high degradation) to  $n_s$  (equal  $r_F^i$  values, low degradation).

We now state our algorithm (pseudocode given in [26]): at each iteration, an equal number of independent forward and reverse trajectories are simulated through Eqs. (6) and (15) using the  $U_F, U_R$  specified by current parameters  $\theta_{\text{curr}}$ , with the time-asymmetric work  $W$  and auxiliary variables  $(\mathbf{a}, \mathbf{b}, \mathbf{c}, \tilde{\mathbf{a}}, \tilde{\mathbf{b}}, \tilde{\mathbf{c}})$  of each trajectory dynamically calculated; then the protocol is updated through solving the nonlinear constrained optimization problem

$$\theta_{\text{next}} = \operatorname{argmin}_{\theta} \{ \hat{J}(\theta) \mid \{n_F^{\text{eff}}(\theta), n_R^{\text{eff}}(\theta)\} \geq f n_s \}, \quad (27)$$

for which there are efficient numerical solvers (e.g. SLSQP [27] pre-implemented in SciPy [28]). Here  $\hat{J}(\theta) = \hat{J}_F(\theta) + \hat{J}_R(\theta)$ ,  $n_F^{\text{eff}}(\theta)$  and  $n_R^{\text{eff}}(\theta)$  are constructed with the  $n_s$  forward and  $n_s$  reverse samples collected over all iterations, and  $f \in [0, 1]$  is a hyperparameter specifying the constraint strength: the fraction of total samples we are constraining  $n_{F,R}^{\text{eff}}$  to be greater or equal than. Finally,  $\widehat{\Delta F}_{\text{BAR}}$  is calculated with the bi-directional work measurements collected across all iterations using Eq. (4), which is permitted by the satisfaction of Eq. (5).

*Numerical examples.*—In this section we report the performance of our algorithm for three test model systems.

We chose our basis set in order to represent protocols of the form

$$U(\mathbf{x}, t) = \lambda_A(t) U_A(\mathbf{x}) + \lambda_B(t) U_B(\mathbf{x}) + \lambda_C(t) U_C(\mathbf{x}) \quad (28)$$

where  $U_C(\mathbf{x})$  is a linear quasi-counterdiabatic potential

$$U_C(\mathbf{x}) = -\mathbf{c} \cdot \mathbf{x} \quad \text{with} \quad \mathbf{c} = \frac{\langle \mathbf{x} \rangle_B - \langle \mathbf{x} \rangle_A}{t_f} \quad (29)$$

directly forcing each coordinate  $x_n$  with magnitude proportional to the difference of its equilibrium values

$\langle \mathbf{x} \rangle_{A,B} = \int \mathbf{x} \rho_{A,B}(\mathbf{x}) d\mathbf{x}$  [29]. The basis set is given by

$$\left\{ U_\ell(\mathbf{x}) p_m \left( \frac{2t}{t_f} - 1 \right) \mid \ell \in \{A, B, C\}, 0 \leq m \leq m_{\max} \right\}, \quad (30)$$

where  $p_m(\cdot)$  is the  $m$ -th Legendre polynomial.

For all numerical examples,  $m_{\max} = 4$  was used and the algorithm was initialized with 120 bi-directional samples drawn from a naive linear interpolation protocol  $\lambda_A(t) = 1 - t/t_f, \lambda_B(t) = t/t_f, \lambda_C(t) = 0$ . At each iteration Eq. (27) was solved for  $n_{\text{mb}} = 20$  independently subsampled minibatches of size  $n_s^{\text{mb}} = 80$  with  $f = 0.3$ ; the protocol was then updated to the minibatch-averaged  $\theta_{\text{next}}$ ; finally, 20 additional bi-directional samples were drawn with the new protocol. In total, 44 iterations were performed, giving 1000 bi-directional samples.

*Linearly-Biased double well.*—The first system we consider is a one-dimensional quartic double-well with a linear bias (Fig. 1(a)). The potentials are  $U_A(x) = E_0[(x^2 - 1)^2/4 - x]$ ,  $U_B(x) = E_0[(x^2 - 1)^2/4 + x]$  (cf. [30] for optimal protocols minimizing  $\langle W_{\text{trad}} \rangle_F$ ). We set  $U_C(x) = 0$  because  $U_B(x) - U_A(x)$  is already linear in  $x$ . We use  $\beta = 1, E_0 = 16$ , and a timestep  $\Delta t = 1 \times 10^{-3}\tau$  where  $\tau = 1$  is the natural timescale (here the length scale, inverse temperature, and friction coefficient are all unity  $\ell = \beta = \gamma = 1$ ).

Fig. 1(b) displays the  $\widehat{\Delta F}_{\text{BAR}}$  estimator mean squared error for 1000 bi-directional work measurements collected solely from the naive protocol (red), the 1000 measurements collected cumulatively over on-the-fly protocol optimization (purple), and 1000 measurements collected solely from the last-iteration (blue). Each dot represents the empirical average over 100 independent trials. Note that the mean squared error is up to 1600 times lower under protocol optimization compared to under the naive protocol (obtained at  $t_f = 0.2$ ). For  $t_f \gtrsim 10$  the algorithm does not converge within the 1000 measurements [26], leading to less improvement. Fig. 1(c) shows that bi-directional work measurements collected under the protocol optimization algorithm have significantly more overlap than measurements collected from the naive protocol, leading to reduced estimator error. Fig. 1(d) gives snapshots on how the optimal protocol is adaptively learned.

*Rouse polymer*—Next we consider a  $(N + 1)$ -bead Rouse polymer (Fig. 2(a)) with stiffness  $k$  and intrinsic energy given by  $U_{\text{Rouse}}(x_0, x_1, \dots, x_N) = \sum_{n=0}^{N-1} (k/2)(x_{n+1} - x_n)^2$  from harmonic bonds between adjacent beads [31, 32]. We estimate  $\Delta F$  between a collapsed state (fixing  $x_0 = x_N = 0$ ) and an extended state (fixing  $x_0 = 0, x_N = \lambda_f$ ), so our configuration space is  $\mathbf{x} \in \mathbb{R}^{N-1}$  with potential energies  $U_A(x_1, \dots, x_{N-1}) = U_{\text{Rouse}}(0, x_1, \dots, x_{N-1}, 0)$  and  $U_B(x_1, \dots, x_{N-1}) = U_{\text{Rouse}}(0, x_1, \dots, x_{N-1}, \lambda_f)$ . Equilibrium averages  $\langle x_n \rangle_A = 0, \langle x_n \rangle_B = n\lambda_f/N$  give  $U_C(\mathbf{x}) = -(\lambda_f/Nt_f) \sum_{n=1}^N nx_n$ , and the ground truth is  $\Delta F = F_B - F_A = k\lambda_f^2/(2N)$ . It may be verified that for this problem the time-varying potential energies

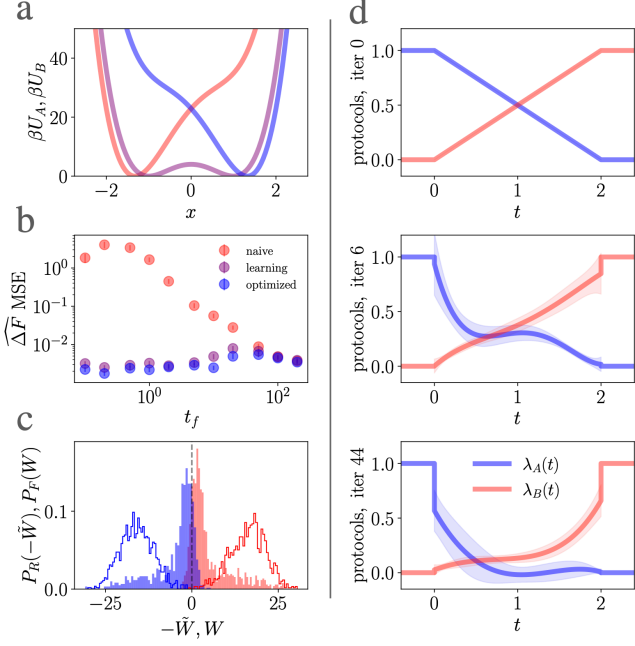


FIG. 1. (a) The potentials  $U_A(\mathbf{x})$  (red) and  $U_B(\mathbf{x})$  (blue) are obtained by linearly biasing a double well (purple). (b)  $\widehat{\Delta F}_{\text{BAR}}$  mean squared error from 1000 bi-directional measurements drawn solely from the naive protocol (red), cumulatively from protocols that are adaptively optimized (“learning”) with our algorithm (purple), and solely from the last-iteration (“optimized”) protocols (blue) for various protocol times  $t_f$ . (c) Single-trial  $P_F(W)$  (red) and  $P_R(-\tilde{W})$  (blue) work distributions for 1000 measurements from the naive protocol, (unfilled) and adaptively optimized protocols (filled) for  $t_f = 2$ , the ground truth shown as a grey dashed line. Measurements made with protocol optimization have significantly more overlap, leading to lower estimator error. (d) Forward protocols  $\lambda_A(t)$  (blue) and  $\lambda_B(t)$  (red) at various iterations of protocol optimization for  $t_f = 2$ . Shaded region represents variability across 100 independent trials. In the optimized last-iteration protocol,  $\lambda_A(t) + \lambda_B(t)$  (giving the energy scale) is greatly reduced at intermediate times, while  $\lambda_B(t) - \lambda_A(t)$  (giving the linear bias) is time-asymmetrically shifted. The reverse protocols (not shown here) are similar [26].

$$\begin{aligned} U_0(\mathbf{x}, t) &= \left(1 - \frac{t}{t_f}\right) U_A(\mathbf{x}) + \left(\frac{t}{t_f}\right) U_B(\mathbf{x}) \\ U_1(\mathbf{x}, t) &= U_C(\mathbf{x}) \end{aligned} \quad (31)$$

solve Eq. (9) and are thus counterdiabatic.

We use  $\beta = k = 1$ ,  $N = 20$ , and timestep  $\Delta t = 2.5 \times 10^{-5} \tau_R$  where  $\tau_R = \beta N^2 / \pi^2$  is the Rouse relaxation time [31]. Initial conditions for  $\rho_A(\mathbf{x})$  and  $\rho_B(\mathbf{x})$  were drawn from a normal-modes basis as described in Appendix Sec. ???. Fig. 2(b) shows an improvement of up to 8300 (for  $t_f = 0.5 \tau_R$ ) in  $\widehat{\Delta F}_{\text{BAR}}$  mean squared error between naive and optimized protocols. The counterdiabatic solution Eq. (31) corresponds

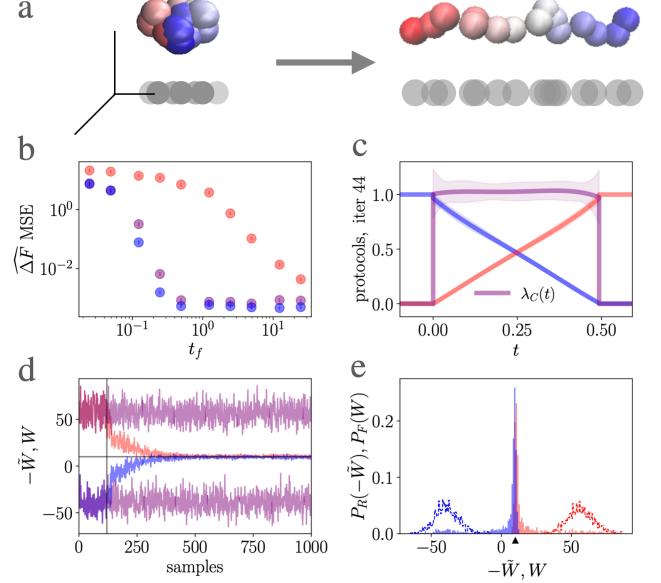


FIG. 2. (a) A Rouse polymer is stretched from a collapsed state to an extended one. (b)  $\widehat{\Delta F}_{\text{BAR}}$  mean squared error versus protocol time, points colored as in Fig. 1. (c) For moderate protocol times ( $t_f = 0.5 \tau_R$  displayed here) the optimized protocol ( $\lambda_A(t), \lambda_B(t), \lambda_C(t)$ ) learned in 44 iterations is the counterdiabatic protocol Eq. (31). (d) Single-trial bi-directional work samples from the naive protocol ( $W$  and  $-\tilde{W}$  purple) and adaptively-optimized protocols ( $W$  red,  $-\tilde{W}$  blue) for  $t_f = 0.5 \tau_R$ . Vertical line demarcates start of protocol optimization. The ground truth  $\Delta F$  is shown as a horizontal line. (e) Work distributions corresponding to the samples in (d). The ground truth is indicated by the triangular arrow. Cumulative measurements made under protocol optimization (filled) have dramatically greater overlap than measurements made under the naive protocols (unfilled), leading to lower estimator error.

to  $\lambda_A(t) = (1 - t/t_f)$ ,  $\lambda_B(t) = t/t_f$ , and  $\lambda_C(t) = 1$ , which is what the algorithm learns for  $t_f = \tau_R$  as depicted in Fig. 2(c). (This was generally the case for  $t_f \geq 0.5 \tau_R$ . For  $t_f < 0.5 \tau_R$  the algorithm learns a sub-optimal local solution that still provides some improvement [26].) Fig. 2(d) shows single-trial traces of bi-directional work measurements for the naive protocol (purple) and adaptively-optimized protocols (red for  $W$ , blue for  $-\tilde{W}$ ), for  $t_f = 0.5 \tau_R$ . The protocol converges in  $\sim 20$  iterations (requiring  $\sim 500$  measurements), and then consistently gives work measurements closely centered at the ground truth free energy (gray horizontal line). Histograms of these traces (filled) are shown in Fig. 2(e), exhibiting a remarkable increase in the overlap compared with their naive counterparts (unfilled).

*Worm-like chain with attractive linker*— We now consider a  $(N + 1)$ -bead worm-like chain model (WLC) in 2 dimensions with an added Lennard-Jones interaction between the first and last beads (similar to the 3rd example of [33]). Fixing  $(x_0, y_0) = (0, 0)$ , the configura-

tion space is  $\vec{\phi} \in \mathbb{R}^N$ , where  $\phi_n$  is the angle of the  $n$ th bond with respect to the  $x$ -axis, with  $(x_n(\vec{\phi}), y_n(\vec{\phi})) = (\sum_{m=1}^n \cos \phi_m, \sum_{m=1}^n \sin \phi_m)$ . The angular potential  $U_\phi = k \sum_{n=1}^{N-1} [1 - \cos(\phi_{n+1} - \phi_n)]$  penalizes the bending of adjacent bonds, and  $U_{\text{LJ}} = 4\epsilon_{\text{LJ}}[(\sigma_{\text{LJ}}/r_N)^{12} - (\sigma_{\text{LJ}}/r_N)^6]$  specifies the interaction between first and last beads, where  $r_N = \sqrt{x_N^2 + y_N^2}$  is the end-to-end distance. We take  $k = 6$ ,  $\beta = 1$ ,  $\epsilon_{\text{LJ}} = 8$ ,  $\sigma_{\text{LJ}} = 4$ , and  $N = 15$ .

Fig. 3(a) displays the conditioned free energy  $F(R/N) := -\beta^{-1} \ln \rho_{\text{eq}}(r_N = R)$ , where  $\rho_{\text{eq}}$  is the equilibrium probability of observing the end-to-end distance under  $U = U_\phi + U_{\text{LJ}}$  [34] (constructed from  $10^7$  equilibrium samples of  $U_\phi$ , obtained with the Metropolis-adjusted Langevin Algorithm [35], that were reweighted by  $U_{\text{LJ}}$ ).  $F(R/N)$  exhibits a deep well for  $R_A \approx 2^{1/6} \sigma_{\text{LJ}}$  (trapped/bent state) and a shallow well at large  $R_B \approx 0.9 N$  (free/relaxed state), separated by a barrier; their difference in value  $\Delta F \approx 4.18$  may be calculated by estimating the  $\Delta F$  between  $U_A(\vec{\phi}) = U_\phi + U_{\text{LJ}} + (k_{\text{ext}}/2)(r_N - \lambda_i)^2$  and  $U_B(\vec{\phi}) = U_\phi + U_{\text{LJ}} + (k_{\text{ext}}/2)(r_N - \lambda_f)^2$  for  $\lambda_i = 2^{1/6} \sigma_{\text{LJ}}$ ,  $\lambda_f = 0.9 N$ , and  $k_{\text{ext}} \gg 1$ .

We calculate the  $\Delta F$  between  $U_A$  and  $U_B$  for  $k_{\text{ext}} = 200$ . We use timestep  $\Delta t = 1.41 \times 10^{-4} \tau_{\text{LJ}}$  where  $\tau_{\text{LJ}} = \sqrt{\epsilon_{\text{LJ}}/\sigma^2}$  is the Lennard-Jones timescale. We use  $U_C(\vec{\phi}) = -\sum_n c_n r_n$ , radially pulling on each individual bead, constructed with  $c_n = (\langle r_n \rangle_B - \langle r_n \rangle_A)/t_f$  from equilibrium samples of  $\rho_A$  and  $\rho_B$ . Fig. 3(b) displays single-trial work histograms for  $t_f = 0.71 \tau_{\text{LJ}}$ , showing work measurements much closer to the ground truth with protocol optimization, compared to the naive protocol. Fig. 3(c) shows the updating  $\widehat{\Delta F}_{\text{BAR}}$  estimator over 100 independent trials converges substantially faster to the ground truth. With 1000 bi-directional samples under the naive protocol the mean squared error is  $1.62 (k_B T)$ ; under protocol optimization, only 160 samples (i.e., just after two iterations of protocol optimization) are required to have a smaller mean squared error. Over various  $t_f$ , the mean squared error is up to 120 times lower under protocol optimization compared to under the naive protocol [26].

*Discussion.*—In this Letter we have demonstrated the microscopic fluctuation theorem for the time-asymmetric work and proposed an on-the-fly time-asymmetric protocol optimization algorithm whose effectiveness we illustrated with three toy models of varying complexity. Time-asymmetric protocols have been considered before [36–38], but to our knowledge we are the first to use  $\widehat{\Delta F}_{\text{BAR}}$  on bi-directional work measurements from adaptive time-asymmetric protocols. A clear next step is to test our algorithm on more physically realistic systems. This work should be straightforward to implement with JAX-MD [39]. In principle our algorithm should work with underdamped dynamics [37], and it should also be possible to adaptively optimize the protocol time  $t_f$  and sampling ratio  $n_F/n_R$ . Another future direction to pursue is to differentially weight early versus later samples in the estimator to account for differences in the variance

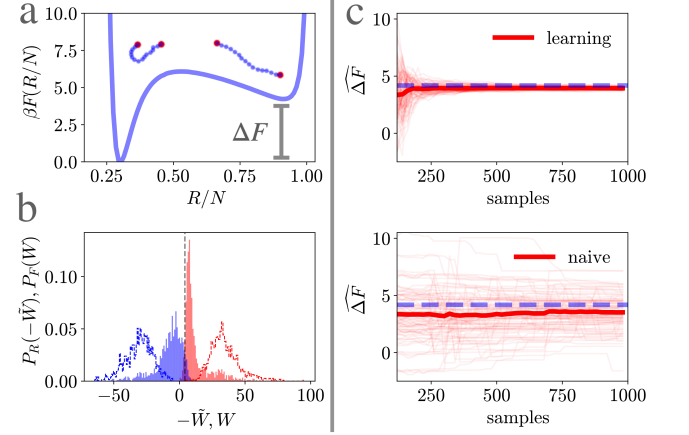


FIG. 3. Worm-like chain with an attractive linker. (a) Ground truth free energy surface relative to its value at  $R_A = 2^{1/6} \sigma_{\text{LJ}}$ ; the left well corresponds to the ends of the chain bound to one another and the right well corresponds to a nearly straight configuration, with a free energy difference  $\Delta F \approx 4.18$ . (b) Work distributions before (unfilled) and during (filled) optimization for  $t_f = 0.71$ , the ground truth shown as a grey dashed line. (c) The  $\widehat{\Delta F}_{\text{BAR}}$  estimator updated over the 1000 samples converges to the ground truth value (dashed blue line) much more quickly under protocol optimization than under the naive protocol. At 1000 samples the protocol optimization free energy estimate was  $\widehat{\Delta F} = 3.94 \pm 0.11$ , while for the naive protocol was  $\widehat{\Delta F} = 3.52 \pm 1.48$  (c.f. ground truth value of  $\Delta F = 4.18$ ). It took 200 total samples for the mean squared error to drop below  $1.00 (k_B T)$  under protocol optimization.

of work measurements, as the algorithm more closely approximates the counterdiabatic protocol.

There are significant ties between our work, and that of “Stochastic Normalizing Flows” [40], wherein authors also consider constructing counterdiabatic protocols, with their “deterministic invertible functions” at every time step corresponding to  $U_1$  in this work. It may be shown that perfect counterdiabatic protocols are perfect stochastic normalizing flows, and they report (after sufficient training) excellent numerical results for free energy estimation. The primary difference is that in their work they fix  $U_0 = (1 - t/t_f)U_A + (t/t_f)U_B$  and use a normal network ansatz (in particular the RealNVP architecture [41]) to learn  $U_1$  for each time-step, whereas here we use a reinforcement learning importance sampling algorithm with a linear set of spatio-temporal basis functions as our ansatz for both  $U_0$  and  $U_1$ . It may be profitable to combine ideas between normalizing flows and time-asymmetric protocols for future studies.

The fast convergence in our method comes from exploiting of the quadratic structure of the Onsager-Machlup path action to construct  $\hat{J}(\theta)$ , which allows all samples to be used in each optimization step. Typically the most computationally expensive step in a molecular dynamics simulation is calculating potential energy

gradients  $\nabla U$  to evolve  $\mathbf{x}(t)$ , which does not need to be repeated to evolve  $(\mathbf{a}_{\mu\nu}, \mathbf{b}_\mu, \dots)$ . A valid critique of our algorithm is that the number of auxiliary variables included with each trajectory scales quadratically with the number of basis functions, becoming prohibitively large when considering, for example, a separate control force on each particle of a many particle system. However, we have shown that a small number of basis functions to represent Eq. (28) already produces a substantial improvement in efficiency for our three examples. That said, it is straightforward to add additional basis functions (cf. Eq. (2) of [42]), which may be useful for more complex and realistic systems. It would be interesting to apply recent methods [43] to learn the optimal set of additional basis functions, that apply force along specific coordinates: bonds, angles, native contacts and other collective variables to further improve performance for larger scale systems.

Documented code for this project may be found at <https://github.com/adrizhong/dF-protocol-optimization>.

## ACKNOWLEDGMENTS

The authors would like to thank Nilesh Tripuraneni, Hunter Akins, Chris Jarzynski, Gavin Crooks, Steve Strong, and the participants of the “Optimal Transport Theory and Applications to Physics” workshop in Les Houches for useful discussions; Jorge L. Rosa-Raíces for helpful comments on an earlier manuscript version; and Evie Pai for lending personal computing resources. This research used the Savio computational cluster resource provided by the Berkeley Research Computing program at the University of California, Berkeley (supported by the University of California Berkeley Chancellor, Vice Chancellor for Research, and Chief Information Officer). AZ is supported by the Department of Defense (DoD) through the National Defense Science & Engineering Graduate (NDSEG) Fellowship Program. BKS is supported by the Kavli Energy Nanoscience institute through the Philomathia Foundation Fellowship. MRD thanks Steve Strong and Fenrir LLC for supporting this

project. This work was supported in part by the U.S. Army Research Laboratory and the U.S. Army Research Office under contract W911NF-20-1-0151.

## Appendix A: Microscopic fluctuation theorem

### 1. The Onsager-Machlup Action

For overdamped Langevin dynamics for  $\mathbf{x} \in \mathbb{R}^d$ ,

$$\dot{\mathbf{x}} = -\nabla U(\mathbf{x}, t) + \sqrt{2\beta^{-1}} \boldsymbol{\eta}(t) \quad \text{with} \quad \mathbf{x}(0) \sim \rho(\cdot), \quad (\text{A1})$$

where  $\boldsymbol{\eta}(t)$  is an instantiation of standard Gaussian white noise with statistics  $\langle \eta_i(t) \rangle = 0$  and  $\langle \eta_i(t) \eta_j(t') \rangle = \delta_{ij} \delta(t - t')$ , and  $\rho(\cdot)$  is its initial distribution, the formal expression for the probability of a path's realization is (up to a multiplicative factor)

$$P[\mathbf{x}(t)] = \rho(\mathbf{x}(0)) e^{-\beta S[\mathbf{x}(t)]}. \quad (\text{A2})$$

Here  $S[\mathbf{x}(t)]$  is the Onsager-Machlup Path Action functional

$$S[\mathbf{x}(t)] = (\text{I}) \int_0^{t_f} \frac{|\dot{\mathbf{x}}(t) + \nabla U(\mathbf{x}(t), t)|^2}{4} dt \quad (\text{A3})$$

which comes from the path discretization into  $N$  timesteps with timestep  $\Delta t = t_f/N$ :  $\mathbf{x}(t) \rightarrow [\mathbf{x}_0, \mathbf{x}_1, \dots, \mathbf{x}_N]$ , with  $\mathbf{x}_n \approx \mathbf{x}(t_n)$ ,  $N = t_f/\Delta t$ , and  $t_n = n\Delta t$ , generated from Euler-Maruyama dynamics

$$\mathbf{x}_0 \sim \rho(\cdot) \quad (\text{A4})$$

$$\mathbf{x}_{n+1} = \mathbf{x}_n - \nabla U(\mathbf{x}_n, t_n) \Delta t + \sqrt{2\beta^{-1}} \Delta \mathbf{B}_n, \quad (\text{A5})$$

where  $\Delta \mathbf{B}_n \sim \mathcal{N}(0, \Delta t I_d)$  is a  $d$ -dimensional Gaussian random variable (i.e., Brownian increment) [17].

The probability of the realization of a particular path is then

$$\begin{aligned} P(\mathbf{x}_0, \mathbf{x}_1, \dots, \mathbf{x}_N) &= P(\mathbf{x}_0) P(\mathbf{x}_1 | \mathbf{x}_0) P(\mathbf{x}_2 | \mathbf{x}_1) \dots P(\mathbf{x}_N | \mathbf{x}_{N-1}) \\ &= \rho(\mathbf{x}_0) \prod_{n=0}^{N-1} (4\pi\beta^{-1}\Delta t)^{-d/2} \exp\left(-\frac{|\mathbf{x}_{n+1} - \mathbf{x}_n + \nabla U(\mathbf{x}_n, t_n)\Delta t|^2}{4\beta^{-1}\Delta t}\right) \\ &\propto \rho(\mathbf{x}_0) \exp\left(-\beta \sum_{n=0}^{N-1} \frac{|(\frac{\mathbf{x}_{n+1}-\mathbf{x}_n}{\Delta t}) + \nabla U(\mathbf{x}_n, t_n)|^2}{4} \Delta t\right), \end{aligned} \quad (\text{A6})$$

where the normalization factor  $(4\pi\beta^{-1}\Delta t)^{-Nd/2}$  is hid-

den in the last line.

Taking  $N \rightarrow \infty$  with  $\Delta t = t_f/N \rightarrow 0$ , the sum within the exponential becomes

$$\begin{aligned} & \sum_{n=0}^{N-1} \frac{|(\frac{\mathbf{x}_{n+1}-\mathbf{x}_n}{\Delta t}) + \nabla U(\mathbf{x}_n, t_n)|^2}{4} \Delta t \\ \rightarrow & \text{(I)} \int_0^{t_f} \frac{|\dot{\mathbf{x}}(t) + \nabla U(\mathbf{x}(t), t)|^2}{4} dt = S[\mathbf{x}(t)], \end{aligned} \quad (\text{A7})$$

which yields the formal expression Eq. (A2).

## 2. Stochastic Integrals and Itô's formula

Here we briefly review the rules of stochastic calculus. For a stochastic path (i.e., a “Brownian motion”  $\mathbf{x}(t)|_{t \in [0, t_f]}$  from Eq. (A1) and some vector-valued function  $F(\mathbf{x}, t)$ , the three following choices for the time-discretization of the integral  $\int_0^{t_f} F(\mathbf{x}(t), t) \cdot \dot{\mathbf{x}}(t) dt$  :

$$\begin{aligned} & \sum_{n=0}^{N-1} F(\mathbf{x}_n, t_n) \cdot \Delta \mathbf{x}_n, \\ & \sum_{n=0}^{N-1} F(\mathbf{x}_{n+\frac{1}{2}}, t_{n+\frac{1}{2}}) \cdot \Delta \mathbf{x}_n, \\ & \sum_{n=0}^{N-1} F(\mathbf{x}_{n+1}, t_{n+1}) \cdot \Delta \mathbf{x}_n \end{aligned}$$

and

$$\sum_{n=0}^{N-1} F(\mathbf{x}_{n+1}, t_{n+1}) \cdot \Delta \mathbf{x}_n$$

(here  $\Delta \mathbf{x}_n = (\mathbf{x}_{n+1} - \mathbf{x}_n)$ ,  $\mathbf{x}_{n+\frac{1}{2}} = (\mathbf{x}_n + \mathbf{x}_{n+1})/2$ , and  $t_{n+\frac{1}{2}} = (t_n + t_{n+1})/2$ ) do *not* necessarily converge to the same value under the  $N \rightarrow \infty$ ,  $\Delta t = t_f/N \rightarrow 0$  limit. This is in contrast to the case where  $\mathbf{x}(t)|_{t \in [0, t_f]}$  is continuously differentiable, e.g., the solution of a well-behaved *deterministic* differential equation, in which case the above three time-discretizations do converge to the same integral value under the limit [44].

Therefore, for trajectories  $\mathbf{x}(t)|_{t \in [0, t_f]}$  obtained through the stochastic differential equation Eq. (A1), we must define each of these as distinct integrals

$$\begin{aligned} \text{(I)} \int_0^{t_f} F(\mathbf{x}, t) \cdot \dot{\mathbf{x}} dt &:= \lim_{N \rightarrow \infty} \sum_{n=0}^{N-1} F(\mathbf{x}_n, t_n) \cdot \Delta \mathbf{x}_n, \\ \text{(S)} \int_0^{t_f} F(\mathbf{x}, t) \cdot \dot{\mathbf{x}} dt &:= \lim_{N \rightarrow \infty} \sum_{n=0}^{N-1} F(\mathbf{x}_{n+\frac{1}{2}}, t_{n+\frac{1}{2}}) \cdot \Delta \mathbf{x}_n, \end{aligned}$$

and

$$\text{(BI)} \int_0^{t_f} F(\mathbf{x}, t) \cdot \dot{\mathbf{x}} dt := \lim_{N \rightarrow \infty} \sum_{n=0}^{N-1} F(\mathbf{x}_{n+1}, t_{n+1}) \cdot \Delta \mathbf{x}_n,$$

which are the Itô, Stratonovich, and Backwards Itô integrals, respectively. They are related to one another by Itô's formula [45]

$$\begin{aligned} & \text{(I)} \int_0^{t_f} F(\mathbf{x}, t) \cdot \dot{\mathbf{x}} + \beta \nabla \cdot F(\mathbf{x}, t) dt \\ &= \text{(S)} \int_0^{t_f} F(\mathbf{x}, t) \cdot \dot{\mathbf{x}} dt \\ &= \text{(BI)} \int_0^{t_f} F(\mathbf{x}, t) \cdot \dot{\mathbf{x}} - \beta \nabla \cdot F(\mathbf{x}, t) dt. \end{aligned} \quad (\text{A8})$$

The Stratonovich integration convention (i.e., with the time-symmetric midpoint-rule discretization) is particularly convenient because ordinary calculus rules (e.g., the chain rule, product rule, etc.) apply.

Note that the three separate time-discretizations of integrals of the form  $\int_0^{t_f} f(\mathbf{x}(t), t) dt$  :

$$\begin{aligned} & \sum_{n=0}^{N-1} f(\mathbf{x}_n, t_n) \Delta t, \\ & \sum_{n=0}^{N-1} f(\mathbf{x}_{n+\frac{1}{2}}, t_{n+\frac{1}{2}}) \Delta t, \\ & \sum_{n=0}^{N-1} f(\mathbf{x}_{n+1}, t_{n+1}) \Delta t \end{aligned}$$

and

$$\sum_{n=0}^{N-1} f(\mathbf{x}_{n+1}, t_{n+1}) \Delta t$$

do converge to the same value under the  $N \rightarrow \infty$  with  $\Delta t = t_f/N \rightarrow 0$  limit, thus  $\text{(I)} \int_0^{t_f} f(\mathbf{x}, t) dt = \text{(S)} \int_0^{t_f} f(\mathbf{x}, t) dt = \text{(BI)} \int_0^{t_f} f(\mathbf{x}, t) dt$ .

## 3. Microscopic fluctuation theorem derivation

Here, we use the stochastic calculus reviewed above to derive Eq. (13), i.e., the equivalence of its first and second lines. We start by manipulating the expression within the exponent

$$\begin{aligned}
U_A(\mathbf{x}(0)) + S[\mathbf{x}(t)] + W[\mathbf{x}(t)] &= U_B(\mathbf{x}(t_f)) + (\text{I}) \int_0^{t_f} \left\{ \frac{|\dot{\mathbf{x}} + \nabla(U_0 + U_1)|^2}{4} - (\dot{\mathbf{x}} + \nabla U_1) \cdot \nabla U_0 + \beta^{-1} \nabla^2(U_1 - U_0) \right\} dt \\
&= U_B(\mathbf{x}(t_f)) + \frac{1}{4}(\text{I}) \int_0^{t_f} |\dot{\mathbf{x}}|^2 dt + \frac{1}{4}(\text{I}) \int_0^{t_f} |\nabla(U_1 - U_0)|^2 dt + \frac{1}{2}(\text{I}) \int_0^{t_f} \dot{\mathbf{x}} \cdot \nabla(U_1 - U_0) + 2\beta \nabla^2(U_1 - U_0) dt \\
&= U_B(\mathbf{x}(t_f)) + \frac{1}{4}(\text{BI}) \int_0^{t_f} |\dot{\mathbf{x}}|^2 dt + \frac{1}{4}(\text{BI}) \int_0^{t_f} |\nabla(U_1 - U_0)|^2 dt + \frac{1}{2}(\text{BI}) \int_0^{t_f} \dot{\mathbf{x}} \cdot \nabla(U_1 - U_0) dt \\
&= U_B(\mathbf{x}(t_f)) + (\text{BI}) \int_0^{t_f} \frac{|\dot{\mathbf{x}} + \nabla(U_1 - U_0)|^2}{4} dt \\
&= U_B(\tilde{\mathbf{x}}(0)) + (\text{I}) \int_0^{t_f} \frac{|-\dot{\tilde{\mathbf{x}}} + \nabla(\tilde{U}_1 - \tilde{U}_0)|^2}{4} dt \\
&= U_B(\tilde{\mathbf{x}}(0)) + \tilde{S}[\tilde{\mathbf{x}}(t)], \quad \text{where } \tilde{S}[\tilde{\mathbf{x}}(t)] = (\text{I}) \int_0^{t_f} \frac{|\dot{\tilde{\mathbf{x}}} + \nabla(\tilde{U}_0 - \tilde{U}_1)|^2}{4} dt. \tag{A9}
\end{aligned}$$

The second equality follows from standard algebraic manipulation. The third equality comes from converting the Forward Itô integrals (I) to Backward Itô integrals (BI) using Itô's formula Eq. (A8). The fourth equality results from standard algebraic manipulation. The fifth equality comes from the time-reversal transformation  $t \rightarrow t_f - t$ , with the Backward Itô integral becoming a forward Itô integral under time-reversal.

Finally, we plug in the above to the first line of Eq. (13) to obtain

$$\begin{aligned}
\tilde{P}[\tilde{\mathbf{x}}(t)] &= e^{-\beta\{U_A(\mathbf{x}(0)) - F_A + S[\mathbf{x}(t)] + W[\mathbf{x}(t)] - \Delta F\}} \\
&= e^{-\beta\{U_B(\tilde{\mathbf{x}}(0)) - F_B + \tilde{S}[\tilde{\mathbf{x}}(t)]\}} \\
&= \rho_B(\tilde{\mathbf{x}}(0)) e^{-\beta\tilde{S}[\tilde{\mathbf{x}}(t)]}, \tag{A10}
\end{aligned}$$

thus completing our derivation.

## Appendix B: Deriving the fluctuation theorem from the microscopic fluctuation theorem

In this section we derive the Crooks Fluctuation Theorem

$$\frac{P_F(+W)}{P_R(-W)} = e^{+\beta(W - \Delta F)} \tag{B1}$$

from the microscopic fluctuation theorem

$$P[\mathbf{x}(t)] e^{-\beta W[\mathbf{x}(t)]} = \tilde{P}[\tilde{\mathbf{x}}(t)] e^{-\beta \Delta F}. \tag{B2}$$

We begin by recalling that  $P_F(\cdot)$ , giving the probability of observing a particular work value in the forward ensemble, is defined as

$$\begin{aligned}
P_F(W') &= \langle \delta(W - W') \rangle_F \\
&= \int D\mathbf{x}(t) P[\mathbf{x}(t)] \delta(W[\mathbf{x}(t)] - W'), \tag{B3}
\end{aligned}$$

where we write  $W'$  to distinguish the argument of  $P_F(\cdot)$  from the path-functional work  $W = W[\mathbf{x}(t)]$ . Here  $D\mathbf{x}(t)$  denotes an integral over all paths  $\mathbf{x}(t)|_{t \in [0, t_f]}$ ,  $P[\mathbf{x}(t)]$  is the probability of its realization, and  $\delta(\cdot)$  is the Dirac-delta function. Plugging in Eq. (B2) to the above expression, we get

$$\begin{aligned}
P_F(W') &= \int D\mathbf{x}(t) \tilde{P}[\tilde{\mathbf{x}}(t)] e^{+\beta\{W[\mathbf{x}(t)] - \Delta F\}} \delta(W[\mathbf{x}(t)] - W') \\
&= e^{+\beta(W' - \Delta F)} \int D\mathbf{x}(t) \tilde{P}[\tilde{\mathbf{x}}(t)] \delta(W[\mathbf{x}(t)] - W') \\
&= e^{+\beta(W' - \Delta F)} \int D\tilde{\mathbf{x}}(t) \tilde{P}[\tilde{\mathbf{x}}(t)] \delta(-\tilde{W}[\tilde{\mathbf{x}}(t)] - W') \\
&= e^{+\beta(W' - \Delta F)} P_R(-W'), \tag{B4}
\end{aligned}$$

where in the second line we pull out the exponential using the Dirac delta function, in the third line we consider the coordinate change  $\mathbf{x}(t) \rightarrow \tilde{\mathbf{x}}(t)$  (using also  $\tilde{W}[\tilde{\mathbf{x}}(t)] = -W[\mathbf{x}(t)]$ , see Eq. (16) and the text that follows it in the main article), and in the fourth line we have recognized that the path integral expression is equivalent to the probability of observing the work value  $-W'$  in the reverse path ensemble.

[1] Z. Cournia, B. Allen, and W. Sherman, Journal of chemical information and modeling **57**, 2911 (2017).

[2] G. Tawa, I. Topol, S. Burt, R. Caldwell, and A. Rashin,

The Journal of Chemical Physics **109**, 4852 (1998).

[3] C. P. Kelly, C. J. Cramer, and D. G. Truhlar, The Journal of Physical Chemistry B **110**, 16066 (2006).

[4] C. Chipot and A. Pohorille, *Free energy calculations*, Vol. 86 (Springer, 2007).

[5] M. R. Shirts, D. L. Mobley, and S. P. Brown, Drug Design **1**, 61 (2010).

[6] Z. Cournia, C. Chipot, B. Roux, D. M. York, and W. Sherman, in *Free Energy Methods in Drug Discovery: Current State and Future Directions* (ACS Publications, 2021) pp. 1–38.

[7] M. R. Shirts and V. S. Pande, The Journal of chemical physics **122**, 144107 (2005).

[8] M. R. Shirts, E. Bair, G. Hooker, and V. S. Pande, Physical review letters **91**, 140601 (2003).

[9] C. H. Bennett, Journal of Computational Physics **22**, 245 (1976).

[10] G. E. Crooks, Journal of Statistical Physics **90**, 1481 (1998).

[11] G. E. Crooks, Physical Review E **60**, 2721 (1999).

[12] S. Vaikuntanathan and C. Jarzynski, Physical Review Letters **100**, 190601 (2008).

[13] Typically there is a factor of the friction coefficient  $\gamma$  multiplying the left side of (6). For notational simplicity we have set it to one, which given that it is equal for all dimensions may always be done through a time-rescaling.

[14] E. Ilker, Ö. Güngör, B. Kuznets-Speck, J. Chiel, S. Deffner, and M. Hinczewski, Physical Review X **12**, 021048 (2022).

[15] S. Iram, E. Dolson, J. Chiel, J. Pelesko, N. Krishnan, Ö. Güngör, B. Kuznets-Speck, S. Deffner, E. Ilker, J. G. Scott, *et al.*, Nature Physics **17**, 135 (2021).

[16] A. G. Frim, A. Zhong, S.-F. Chen, D. Mandal, and M. R. DeWeese, Physical Review E **103**, L030102 (2021).

[17] A. B. Adib, The Journal of Physical Chemistry B **112**, 5910 (2008).

[18] J. Tang and P. Abbeel, Advances in Neural Information Processing Systems **23** (2010).

[19] The astute reader might point out that under the rules of stochastic calculus, how they are written out  $a = \dot{a}$  for all  $\mathbf{x}(t)$ . However, they are different under a finite time-discretization, and thus must both be kept track.

[20] R. J. Williams, Reinforcement learning , 5 (1992).

[21] J. Peters and S. Schaal, Neural networks **21**, 682 (2008).

[22] P. B. Warren and R. J. Allen, Physical review letters **109**, 250601 (2012).

[23] A. Das and D. T. Limmer, The Journal of chemical physics **151**, 244123 (2019).

[24] A. Das, B. Kuznets-Speck, and D. T. Limmer, Physical Review Letters **128**, 028005 (2022).

[25] A. B. Owen, *Monte Carlo theory, methods and examples* (2013).

[26] Supplementary material currently in preparation.

[27] D. Kraft, Forschungsbericht- Deutsche Forschungs- und Versuchsanstalt fur Luft- und Raumfahrt (1988).

[28] P. Virtanen, R. Gommers, T. E. Oliphant, M. Haberland, T. Reddy, D. Cournapeau, E. Burovski, P. Peterson, W. Weckesser, J. Bright, S. J. van der Walt, M. Brett, J. Wilson, K. J. Millman, N. Mayorov, A. R. J. Nelson, E. Jones, R. Kern, E. Larson, C. J. Carey, I. Polat, Y. Feng, E. W. Moore, J. VanderPlas, D. Laxalde, J. Perktold, R. Cimrman, I. Henriksen, E. A. Quintero, C. R. Harris, A. M. Archibald, A. H. Ribeiro, F. Pedregosa, P. van Mulbregt, and SciPy 1.0 Contributors, Nature Methods **17**, 261 (2020).

[29] The first two terms are a generalization of the protocol form  $U_\lambda(\mathbf{x}) = (1 - \lambda) U_A(\mathbf{x}) + \lambda U_B(\mathbf{x})$  commonly considered in stochastic thermodynamics. Typically, linear combinations of just  $U_A(\mathbf{x})$  and  $U_B(\mathbf{x})$  are not effective in transporting  $\rho_A(\mathbf{x}) \rightarrow \rho_B(\mathbf{x})$ , motivating our inclusion of the linear potential  $U_C(\mathbf{x})$ .

[30] A. Zhong and M. R. DeWeese, Physical Review E **106**, 044135 (2022).

[31] M. Doi, S. F. Edwards, and S. F. Edwards, *The theory of polymer dynamics*, Vol. 73 (oxford university press, 1988).

[32] Because of the harmonic nature of the interbead potential, the dynamics of the Rouse polymer separates in its 3 spatial dimensions; without loss of generality, we can consider just a single spatial dimension.

[33] B. Kuznets-Speck and D. T. Limmer, Biophysical Journal **122**, 1659 (2023).

[34] From the change of coordinates  $R = \sqrt{x_N^2 + y_N^2}$ ,  $\vartheta = \tan^{-1}(y_N/x_N)$  and the radial symmetry of  $U_\phi$  and  $U_{\text{LJ}}$ , one has  $\rho_{\text{eq}}(R) \propto (2\pi R)^{-1} \rho_{\text{eq}}(x_N = R, y_N = 0)$ .

[35] G. O. Roberts and R. L. Tweedie, Bernoulli , 341 (1996).

[36] G. Li, H. Quan, and Z. Tu, Physical Review E **96**, 012144 (2017).

[37] G. Li and Z. Tu, Physical Review E **100**, 012127 (2019).

[38] S. Blaber and D. A. Sivak, The Journal of Chemical Physics **153**, 244119 (2020).

[39] S. Schoenholz and E. D. Cubuk, Advances in Neural Information Processing Systems **33**, 11428 (2020).

[40] H. Wu, J. Köhler, and F. Noé, Advances in Neural Information Processing Systems **33**, 5933 (2020).

[41] L. Dinh, J. Sohl-Dickstein, and S. Bengio, arXiv preprint arXiv:1605.08803 (2016).

[42] L. N. Naden, T. T. Pham, and M. R. Shirts, Journal of Chemical Theory and Computation **10**, 1128 (2014).

[43] A. N. Singh and D. T. Limmer, arXiv preprint arXiv:2302.14857 (2023).

[44] C. C. Pugh and C. Pugh, *Real mathematical analysis*, Vol. 2011 (Springer, 2002).

[45] B. Oksendal, *Stochastic differential equations: an introduction with applications* (Springer Science & Business Media, 2013).

# Supplementary Information for “Time-Asymmetric Protocol Optimization for Efficient Free Energy Estimation”

Adrienne Zhong,<sup>1, 4</sup> Benjamin Kuznets-Speck,<sup>2, 4</sup> and Michael R. DeWeese<sup>1, 3</sup>

<sup>1</sup>*Department of Physics, University of California, Berkeley, CA, 94720, USA*

<sup>2</sup>*Biophysics Graduate Group, University of California, Berkeley, CA, 94720, USA*

<sup>3</sup>*Redwood Center For Theoretical Neuroscience and Helen Wills Neuroscience Institute, University of California, Berkeley, Berkeley, CA, 94720*

<sup>4</sup>*These authors contributed equally*

(Dated: November 27, 2023)

## I. INITIAL SAMPLES FOR ROUSE POLYMER FROM NORMAL-MODES DECOMPOSITION

For the Rouse polymer, random samples may be drawn by exploiting a normal-modes decomposition. We can write

$$U_{A,B}(x_1, x_2, \dots, x_{N-1}) = \bar{U}\left(x_1 - \frac{\lambda_{i,f}}{N}, x_2 - \frac{2\lambda_{i,f}}{N}, \dots, x_{N-1} - \frac{(N-1)\lambda_{i,f}}{N}\right) + \frac{k\lambda_{i,f}^2}{2N}, \quad (\text{S1})$$

where  $\bar{U}(\vec{y}) = \vec{y}^T K \vec{y} / 2$  with

$$K = \begin{pmatrix} 2k & -k & & & & 0 \\ -k & 2k & -k & & & \\ & -k & \ddots & & & \\ & & \ddots & -k & & \\ 0 & & & -k & 2k & -k \\ & & & & -k & 2k \end{pmatrix}. \quad (\text{S2})$$

Then, we can do an eigenmode decomposition of  $K$ , writing

$$\bar{U}(\vec{y}) = \hat{U}(\vec{z}) = \sum_{n=1}^{N-1} \frac{\kappa_n z_n^2}{2},$$

where

$$\kappa_n = 2 \left[ 1 - \cos \left( \frac{\pi n}{N} \right) \right], \quad (\text{S3})$$

$$z_n = \sqrt{\frac{2}{N}} \sum_{m=1}^{N-1} \sin \left( \frac{2\pi nm}{N} \right) y_m. \quad (\text{S4})$$

Finally, for an individual initial condition, we draw the normal random variable  $z_n \sim \mathcal{N}(\mu = 0, \sigma^2 = (\beta\kappa_n)^{-1})$  for each  $n$ , as  $\hat{\rho}(\vec{z}) \propto \prod \exp(-\beta\kappa_n z_n^2/2)$ ; then we convert from  $\vec{z}$  to  $\vec{y}$  coordinates via

$$y_n = \sqrt{\frac{2}{N}} \sum_{m=1}^{N-1} \sin \left( \frac{2\pi nm}{N} \right) z_m, \quad (\text{S5})$$

before finally adding  $x_n = y_n + n\lambda_{i,f}/N$  to get our initial condition.

Incidentally, the  $k\lambda_{i,f}^2/2N$  in the expression comparing  $U_{A,B}(\vec{x})$  to  $U(\vec{y})$  is, up to an additive constant, the free energy  $F_{A,B}$ .

---

**Algorithm 1** Time-Asymmetric Protocol Optimization via Adaptive Importance Sampling

---

1: **inputs**  $\beta, U_A(\mathbf{x}), U_B(\mathbf{x})$ ; stepsize  $dt$ , number of timesteps  $N$ , basis functions  $\{U_\mu(\mathbf{x}, n)|_{n=1, \dots, N}\}$ , initial guess  $\theta_{\text{init}}$   
2: **parameters** Samples per iteration  $N_s$ , minibatches per iteration  $N_{\text{mb}}$ , minibatch size  $n_s^{\text{mb}}$ , constraint strength  $f$   
3: **given** Methods `DRAWSAMPLEA()`, `DRAWSAMPLEB()` that return equilibrium samples from  $\rho_A, \rho_B$   
4: **output** Iteratively updated  $\widehat{\Delta F}$  estimate  
5:  
6: **function** `RUNTRAJF`(parameters  $\theta = (\theta_F, \theta_R)$ ) ▷ Euler-Maruyama method  
7:   Obtain  $\mathbf{x}_0 \leftarrow \text{DRAWSAMPLEA}()$   
8:   Initialize  $\mathbf{x}, \mathbf{a}_{\mu\nu}, \mathbf{b}_\mu, \tilde{\mathbf{a}}_{\mu\nu}, \tilde{\mathbf{b}}_\mu \leftarrow \mathbf{x}_0, 0, 0, 0, 0$   
9:   **for**  $n = 1, \dots, N$  **do**  
10:     Evaluate  $\nabla U_\mu \leftarrow \nabla U_\mu(\mathbf{x}, n)$  for each  $\mu$   
11:     Calculate  $d\mathbf{x} \leftarrow -\theta_F^\mu \nabla U_\mu dt + \sqrt{2\beta^{-1}} dB$ , where  $dB \sim \mathcal{N}(0, dt \times I_d)$  is a  $d$ -dimensional normal random variable  
12:     Evaluate  $\nabla \tilde{U}_\mu \leftarrow \nabla U_\mu(\mathbf{x} + d\mathbf{x}, n)$  for each  $\mu$   
13:     Evolve  $\mathbf{x} \leftarrow \mathbf{x} + d\mathbf{x}$   
14:     Evolve  $\mathbf{a}_{\mu\nu}, \mathbf{b}_\mu \leftarrow \mathbf{a}_{\mu\nu} + \nabla U_\mu \cdot \nabla U_\nu dt/4, \mathbf{b}_\mu + \nabla U_\mu \cdot d\mathbf{x}/2$   
15:     Evolve  $\tilde{\mathbf{a}}_{\mu\nu}, \tilde{\mathbf{b}}_\mu \leftarrow \tilde{\mathbf{a}}_{\mu\nu} + \nabla \tilde{U}_\mu \cdot \nabla \tilde{U}_\nu dt/4, \tilde{\mathbf{b}}_\mu - \nabla \tilde{U}_\mu \cdot d\mathbf{x}/2$  ▷ This holds because  $d\tilde{\mathbf{x}} = -d\mathbf{x}$   
16:   **end for**  
17:   Evaluate  $\mathbf{c}, \tilde{\mathbf{c}} \leftarrow U_A(\mathbf{x}_0), U_B(\mathbf{x})$   
18:   Calculate  $W \leftarrow -(\theta_F^\mu \theta_F^\nu \mathbf{a}_{\mu\nu} + \theta_F^\mu \mathbf{b}_\mu + \mathbf{c}) + (\theta_R^\mu \theta_R^\nu \tilde{\mathbf{a}}_{\mu\nu} + \theta_R^\mu \tilde{\mathbf{b}}_\mu + \tilde{\mathbf{c}})$   
19:   **return**  $W, \mathbf{a}_{\mu\nu}, \mathbf{b}_\mu, \mathbf{c}, \tilde{\mathbf{a}}_{\mu\nu}, \tilde{\mathbf{b}}_\mu, \tilde{\mathbf{c}}$ ,  $\theta$   
20: **end function**  
21:  
22: **function** `RUNTRAJR`(parameters  $\theta = (\theta_F, \theta_R)$ )  
23:   Obtain  $\tilde{\mathbf{x}}_0 \leftarrow \text{DRAWSAMPLEB}()$   
24:   Initialize  $\tilde{\mathbf{x}}, \tilde{\mathbf{a}}_{\mu\nu}, \tilde{\mathbf{b}}_\mu, \mathbf{a}_{\mu\nu}, \mathbf{b}_\mu \leftarrow \tilde{\mathbf{x}}_0, 0, 0, 0, 0$   
25:   **for**  $n = 1, \dots, N$  **do** ▷ because  $\nabla \tilde{U}_\mu(\cdot, n) = \nabla U_\mu(\cdot, N+1-n)$   
26:     Evaluate  $\nabla \tilde{U}_\mu \leftarrow \nabla U_\mu(\tilde{\mathbf{x}}, N+1-n)$  for each  $\mu$   
27:     Calculate  $d\tilde{\mathbf{x}} \leftarrow -\theta_R^\mu \nabla \tilde{U}_\mu dt + \sqrt{2\beta^{-1}} dB$ , where  $dB \sim \mathcal{N}(0, dt \times I_d)$  is a  $d$ -dimensional normal random variable  
28:     Evaluate  $\nabla U_\mu \leftarrow \nabla U_\mu(\tilde{\mathbf{x}} + d\tilde{\mathbf{x}}, N+1-n)$  for each  $\mu$   
29:     Evolve  $\tilde{\mathbf{x}} \leftarrow \tilde{\mathbf{x}} + d\tilde{\mathbf{x}}$   
30:     Evolve  $\tilde{\mathbf{a}}_{\mu\nu}, \tilde{\mathbf{b}}_\mu \leftarrow \tilde{\mathbf{a}}_{\mu\nu} + \nabla \tilde{U}_\mu \cdot \nabla \tilde{U}_\nu dt/4, \tilde{\mathbf{b}}_\mu + \nabla \tilde{U}_\mu \cdot d\tilde{\mathbf{x}}/2$   
31:     Evolve  $\mathbf{a}_{\mu\nu}, \mathbf{b}_\mu \leftarrow \mathbf{a}_{\mu\nu} + \nabla U_\mu \cdot \nabla U_\nu dt/4, \mathbf{b}_\mu - \nabla U_\mu \cdot d\tilde{\mathbf{x}}/2$   
32:   **end for**  
33:   Evaluate  $\tilde{\mathbf{c}}, \mathbf{c} \leftarrow U_B(\tilde{\mathbf{x}}_0), U_A(\tilde{\mathbf{x}})$   
34:   Calculate  $\tilde{W} \leftarrow -(\theta_R^\mu \theta_R^\nu \tilde{\mathbf{a}}_{\mu\nu} + \theta_R^\mu \tilde{\mathbf{b}}_\mu + \tilde{\mathbf{c}}) + (\theta_F^\mu \theta_F^\nu \mathbf{a}_{\mu\nu} + \theta_F^\mu \mathbf{b}_\mu + \mathbf{c})$   
35:   **return**  $\tilde{W}, \tilde{\mathbf{a}}_{\mu\nu}, \tilde{\mathbf{b}}_\mu, \tilde{\mathbf{c}}, \mathbf{a}_{\mu\nu}, \mathbf{b}_\mu, \mathbf{c}, \theta$   
36: **end function**  
37:  
38: **function** `UPDATETHETA`(forward samples  $\mathcal{S}_F$ , reverse samples  $\mathcal{S}_R$ )  
39:   Initialize  $\mathcal{S}_{\theta, \text{mb}} \leftarrow \{\}$   
40:   **repeat**  $N_{\text{mb}}$  **times** ▷ Use larger  $N_{\text{mb}}$  for larger  $|\mathcal{S}_F|$   
41:     Randomly select  $\mathcal{S}_F^{\text{mb}} \subset \mathcal{S}_F$  of size  $n_s^{\text{mb}}$  without replacement  
42:     Randomly select  $\mathcal{S}_R^{\text{mb}} \subset \mathcal{S}_R$  of size  $n_s^{\text{mb}}$  without replacement  
43:      $\theta^* \leftarrow \text{argmin}_\theta \{ \hat{J}_F(\theta; \mathcal{S}_F^{\text{mb}}) + \hat{J}_R(\theta; \mathcal{S}_R^{\text{mb}}) \mid n_F^{\text{eff}}(\theta; \mathcal{S}_F^{\text{mb}}) \geq fn_s^{\text{mb}}, n_R^{\text{eff}}(\theta; \mathcal{S}_R^{\text{mb}}) \geq fn_s^{\text{mb}} \}$   
44:      $\mathcal{S}_{\theta, \text{mb}}.\text{insert}(\theta^*)$   
45:   **end**  
46:   **return**  $\text{mean}(\mathcal{S}_{\theta, \text{mb}})$   
47: **end function**  
48:  
49: **procedure** `MAIN()`  
50:   Initialize parameters  $\theta \leftarrow \theta_{\text{init}}$  and sample arrays  $\mathcal{S}_F, \mathcal{S}_R \leftarrow \{\}, \{\}$   
51:   **repeat** ▷ Use  $N_{\text{mb}} + N_s$  on first iteration  
52:     **repeat**  $N_s$  **times**  
53:        $\mathcal{S}_F.\text{insert}(\text{RUNTRAJF}(\theta))$   
54:        $\mathcal{S}_R.\text{insert}(\text{RUNTRAJR}(\theta))$   
55:     **end**  
56:     Update estimate  $\widehat{\Delta F} \leftarrow \widehat{\Delta F}_{\text{BAR}}(\mathcal{S}_F, \mathcal{S}_R)$   
57:      $\theta \leftarrow \text{UPDATETHETA}(\mathcal{S}_F, \mathcal{S}_R)$   
58:     **until** out of computer time  
59: **end procedure**


---

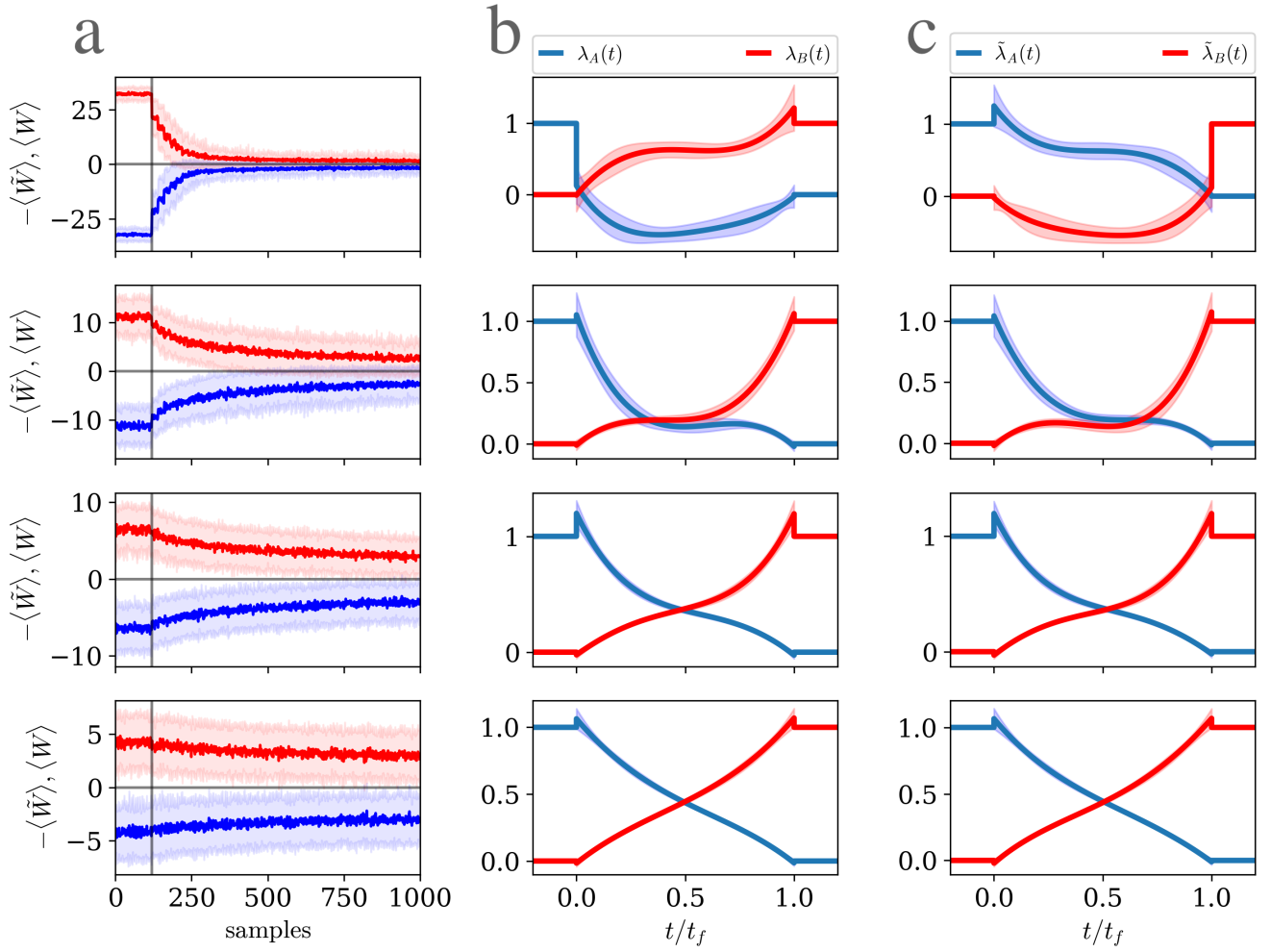


FIG. S1: (a) For the linearly-biased double well, ensemble-averaged work across 100 trials, as a function of sample number. Parameter optimization begins at 120 samples, and happens every 20 samples. The rows correspond to protocol times  $t_f = 0.2, 5.0, 20.0$ , and 50.0 respectively. Convergence is slower for larger  $t_f$ ; for  $t_f = 50.0$  the protocol may not have converged within 1000 samples. (b) The forward protocols  $U_F(\cdot, t) = \lambda_A(t)U_A(\cdot) + \lambda_B(t)U_B(\cdot)$  after 1000 samples. Rows correspond to the same  $t_f$ . (c) The reverse protocols  $U_R(\cdot, t) = \tilde{\lambda}_A(t)U_A(\cdot) + \tilde{\lambda}_B(t)U_B(\cdot)$  after 1000 samples. The reverse protocols appear to satisfy  $\tilde{\lambda}_A(t) = \lambda_B(t_f - t)$  and  $\tilde{\lambda}_B(t) = \lambda_A(t)$ , which is due to the symmetry of  $U_A(\cdot)$  and  $U_B(\cdot)$  in the problem.

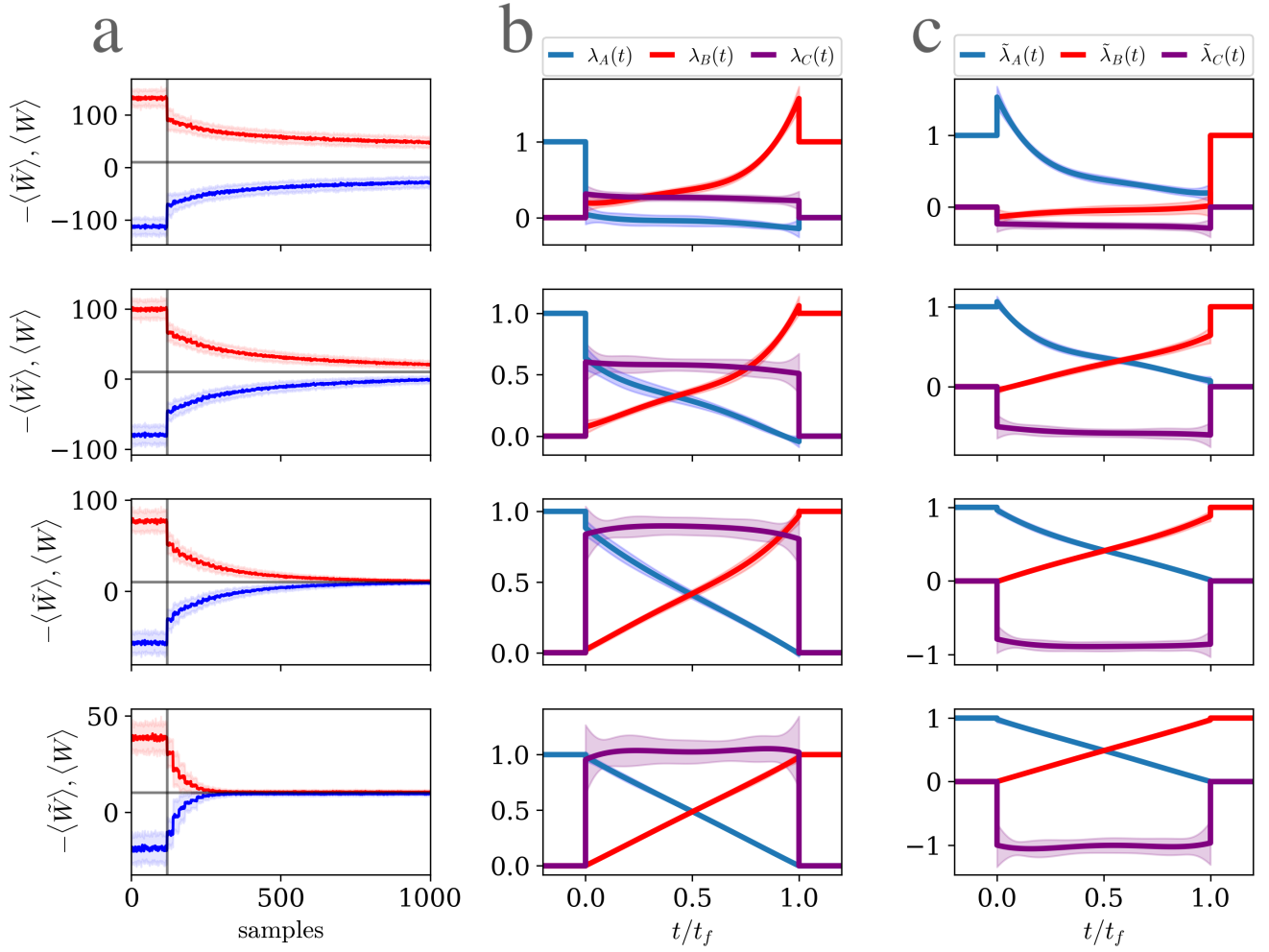


FIG. S2: (a) For the Rouse polymer, ensemble-averaged work across 100 trials, as a function of sample number. Parameter optimization begins at 120 samples, and happens every 20 samples. The rows correspond to protocol times  $t_f = 0.05 \tau_R, 0.12 \tau_R, 0.25 \tau_R, \text{ and } 1.23 \tau_R$  respectively. Unlike for the double well, convergence here is slower for smaller  $t_f$ . (b) The forward protocols  $U_F(\cdot, t) = \lambda_A(t)U_A(\cdot) + \lambda_B(t)U_B(\cdot) + \lambda_C(t)U_C(\cdot)$  after 1000 samples. Rows correspond to the same  $t_f$ . For  $t_f = 0.05 \tau_R$  and  $t_f = 0.12 \tau_R$ , the protocol has not yet converged to the counterdiabatic solution  $\lambda_A(t) = (1 - t/t_f), \lambda_B(t) = t/t_f, \lambda_C = 1$ . (c) The reverse protocols  $U_R(\cdot, t) = \tilde{\lambda}_A(t)U_A(\cdot) + \tilde{\lambda}_B(t)U_B(\cdot) + \tilde{\lambda}_C(t)U_C(\cdot)$  after 1000 samples. The reverse protocols appear to satisfy  $\tilde{\lambda}_A(t) = \lambda_B(t_f - t)$ ,  $\tilde{\lambda}_B(t) = \lambda_A(t)$ , and  $\tilde{\lambda}_C(t) = -\lambda_C(t)$ , which is due to the symmetry of  $U_A(\cdot), U_B(\cdot)$ , and  $U_C(\cdot)$  in the problem.

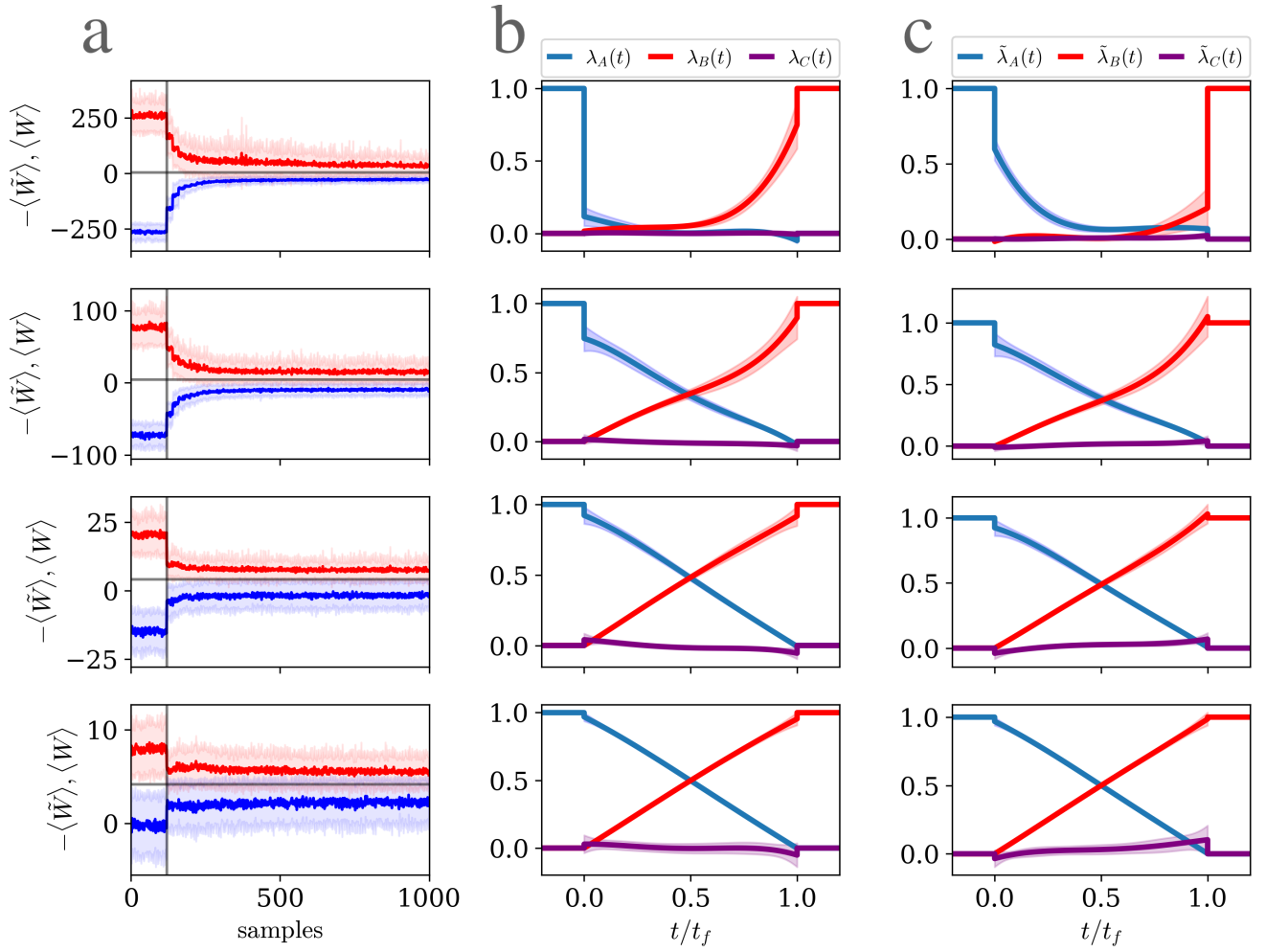


FIG. S3: (a) For the worm-like chain, ensemble-averaged work across 100 trials, as a function of sample number. Parameter optimization begins at 120 samples, and happens every 20 samples. The rows correspond to protocol times  $t_f = 0.07 \tau_{\text{LJ}}, 0.28 \tau_{\text{LJ}}, 1.41 \tau_{\text{LJ}}, \text{ and } 7.07 \tau_{\text{LJ}}$  respectively. It appears convergence is reached rapidly, within the 1000 samples for all cases. (b) The forward protocols  $U_F(\cdot, t) = \lambda_A(t)U_A(\cdot) + \lambda_B(t)U_B(\cdot) + \lambda_C(t)U_C(\cdot)$  after 1000 samples. Rows correspond to the same  $t_f$ . For small  $t_f$ , the protocol has reduced magnitude. This corresponds to lowering the potential, or raising the temperature (i.e., smaller  $\beta U(\cdot, t)$ ). (c) The reverse protocols  $U_R(\cdot, t) = \tilde{\lambda}_A(t)U_A(\cdot) + \tilde{\lambda}_B(t)U_B(\cdot) + \tilde{\lambda}_C(t)U_C(\cdot)$  after 1000 samples. Due to the intrinsic asymmetry of the problem between pulled and collapsed states, the resulting reverse protocols do not obey the symmetries observed in the double-well and Rouse polymer problems.

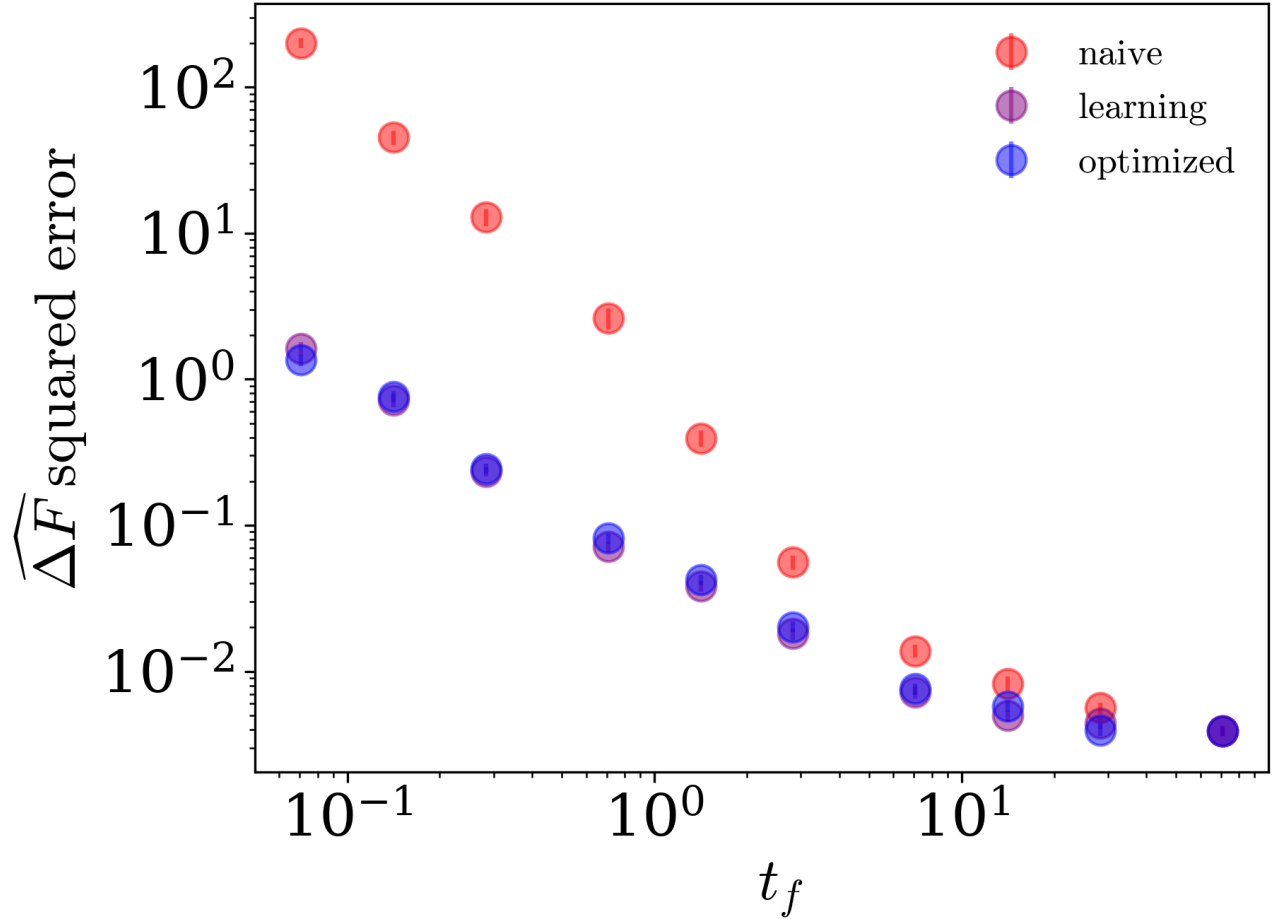


FIG. S4: Performance plot for the worm-like chain. That the mean squared error for protocol learning is near equal to the optimized protocol implies convergence occurs quickly within protocol optimization, cf Fig. S3(a). At  $t_f = 0.07 \tau_{\text{LJ}}$ , the MSE is 123.3 times lower under protocol optimization than under the naive protocol.